Differential Image Based Robot to MRI Scanner Registration with Active Fiducial Markers for an MRI-Guided Robotic Catheter System

E. Erdem Tuna, Nate Lombard Poirot, Juana Barrera Bayona, Dominique Franson, Sherry Huang, Julian Narvaez, Nicole Seiberlich, Mark Griswold, M. Cenk Çavuşoğlu

Abstract—In magnetic resonance imaging (MRI) guided robotic catheter ablation procedures, reliable tracking of the catheter within the MRI scanner is needed to safely navigate the catheter. This requires accurate registration of the catheter to the scanner. This paper presents a differential, multi-slice image-based registration approach utilizing active fiducial coils. The proposed method would be used to preoperatively register the MRI image space with the physical catheter space. In the proposed scheme, the registration is performed with the help of a registration frame, which has a set of embedded electromagnetic coils designed to actively create MRI image artifacts. These coils are detected in the MRI scanner's coordinate system by background subtraction. The detected coil locations in each slice are weighted by the artifact size and then registered to known ground truth coil locations in the catheter's coordinate system via least-squares fitting. The proposed approach is validated by using a set of target coils placed withing the workspace, employing multiplanar capabilities of the MRI scanner. The average registration and validation errors are respectively computed as 1.97 mm and 2.49 mm. The multi-slice approach is also compared to the single-slice method and shown to improve registration and validation by respectively 0.45 mm and 0.66 mm.

I. INTRODUCTION

The magnetic resonance imaging (MRI) guided interventions are getting widespread applications in clinical settings due to MRI's high soft tissue contrast and radiation-free imaging. One such procedure is catheter ablation for the treatment of atrial fibrillation. In this procedure, the catheter is guided by the physician to the left atrium via passing through the femoral vein, the right atrium and the atrial septal wall. In the left atrium, the tip is steered to reach the desired area, such as the ostia of the pulmonary veins, and radio frequency energy is applied to form barriers to prevent the spread of the irregular electrical signals [1].

For the last decade, robotic catheters have emerged as a promising technology for catheter ablation [2]. The development of MRI-guided robotic catheters is complicated by the need to track in real-time the position and orientation of these instruments within the MRI scanner. In order to

Manuscript received September 15, 2019. This work was supported in part by the National Science Foundation under grants CISE IIS-1524363, CISE IIS-1563805, ENG IIP-1700839, and the National Heart, Lung, and Blood Institute of the National Institutes of Health under grant R01 HL153034.

- E. E. Tuna, N. L. Poirot, J. B. Bayona, J. Narvaez, and M. C. Çavuşoğlu are with the Department of Electrical, Computer, and Systems Engineering, Case Western Reserve University, Cleveland, OH 44106, USA (e-mail:eet12@case.edu, njl49@case.edu, jvb26@case.edu, julian.narvaez@case.edu, mcc14@case.edu)
- D. Franson, S. Huang, and M. Griswold are with the Department of Biomedical Engineering, Case Western Reserve University, Cleveland, OH 44106, USA (e-mail:dnf7@case.edu, sxh585@case.edu, mark.griswold@case.edu).
- N. Seiberlich is with the Department of Radiology, University of Michigan, Ann-Anbor, MI 48109, USA (e-mail:nse@med.umich.edu).

navigate such a catheter to a location selected in an MRI image and track catheter's pose, it is necessary to register the robot space to the scanner's image space.

Robot to image registration methods have been previously developed for image-guided interventions. These approaches include utilizing joint encoding [3], [4], passive MRI fiducial markers [5]–[8], optical position sensors [9], gradient field sensing [10], and micro tracking coils [11], [12].

Most common of these methods are using either microtracking coils or passive MRI fiducial markers. Although the coil-based approaches provide real-time registration and have high accuracy, they require custom scanner programming for each scanner and thus are not easily applicable from one scanner to another [5]. Fiducial marker-based methods are scanner independent thus providing portability. Their performance depends on the number and configuration of the markers. The existing methods also rely on specific designs of fiducial frames or MRI sequences [13], [14].

In this paper, a differential image based registration algorithm is presented for the novel steerable robotic catheter system proposed by Liu *et al*. [15]–[17]. A set of active fiducial coils embedded along a registration frame (Fig. 1) are used for the registration of the MRI image space with the physical catheter space. The locations of these coils are known with respect to the robot base from the CAD file that is used to manufacture the frame structure. When the coils are inactive, a multi-slice image is acquired and

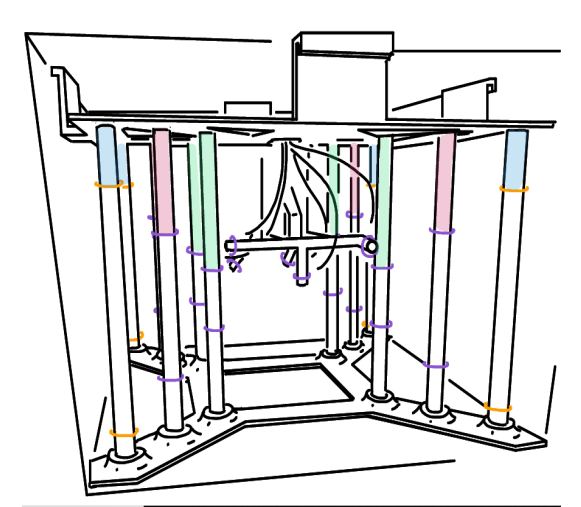


Fig. 1. Schematic of the registration prototype used for the proposed approach. Yellow and purple circles respectively indicate the fiducial coils used for calibration and validation.

used as the background (static) model. Then, the coils are activated by passing currents through and the multi-slice image acquisition is repeated using the same MRI sequence parameters. This multi-slice image is used as the foreground (moving) model. By subtracting the background model from the foreground model, a set of circular imaging artifacts are obtained, which give the location of the fiducial coils along the pillars.

For each coil, its location is computed by a weighted average of detected artifact centroids among slices. The weights correspond to the artifact area in each slice. Artifact centroid and radius in each slice are estimated via Hough transform. Finally, the registration between these two sets of 3 degrees of freedom (DOF) data, namely, coil locations with respect to the scanner image coordinates and coil locations with respect to the physical robot coordinates, is performed by least-squares fitting.

The registration procedure is validated by various target coils placed inside the workspace. In order to eliminate any other errors, such as catheter modeling inaccuracies, and focus only on the registration error, a set coils, with known baseline coordinates, were used as validation targets instead of a catheter prototype.

The related studies regarding robot-imaging modality registration are given in Section II. Proposed differential registration approach is described in Section III. The experimental setup and procedures are explained in Section IV-B and the results are presented in Section IV-C. Finally, the discussions and conclusions are given in Section V.

II. RELATED STUDIES

Reliable instrument tracking and precise targeting during image-guided interventions require accurate image-to-robot registration. Several research groups studied the problem of spatial registration of robotic and manual instruments within imaging modalities and more specifically in MRI-guided procedures. Two most-common approaches are utilizing passive and active fiducial markers for registering instrument coordinate system to the image coordinate system.

The passive fiducial marker based registration methods utilize markers filled with contrast agents, which are detectable by the corresponding imaging modality. Susil $et\,al.$ [8] presented a registration method for CT-guided interventions that uses nine passive fiducial marker tubes, which placed in a Z-frame, and uses one single image for computing the parameters. The method was generalized by Lee $et\,al.$ [7] to an algorithm that allows the registration of a plane to a set of lines.

Tokuda *et al.* [14] proposed an automatic fiducial frame detection and registration based on automatic extraction of linear features to mitigate dependence of Z-frame registration to the thresholding performance. In [6], Shang *et al.* developed multi-image registration method for tracking MRI-guided robots and showed multi-slice method improves accuracy compared to single slice method [8]. This approach is later employed by [18]. Z-frame based instrument to MR scanner registration algorithm is further utilized in [19]–[23].

Other configurations of MR-visible markers are used in [24]–[31] to register needle-guided systems to the image coordinate system. The marker locations in the needle guidance system are known. The instrument coordinate system are registered to the MRI coordinate system after the segmentation and detection of the markers in the MR images.

The active fiducial-based registration method employs a number of micro-tracking coils [11], [32], [33] embedded in the end-effector of the device, which pick up their spatial position in the MRI scanner. It provides high-accuracy and fast registration. However, it requires custom scanner programming and dedicated scanner channels. Currently, a limited number of scanners support micro-tracking coils as a default capability making it challenging to be portable from one scanner to another.

In this paper, an alternative robot to MRI scanner registration approach is presented. Unlike the Z-frame method, it does not rely on specific designs of fiducial frames or thresholding and unlike the micro-tracking method, it does not require custom scanner programming, receiver channel reservation, or complicated instrument design. Eight active fiducial coils are embedded on a frame and placed inside the workspace. The locations of these coils in MR images are detected by background subtraction and using standard imaging pulse sequences. The detected coils are registered to their known ground truth locations in catheter base coordinate system by least square fitting.

The method is validated on a set of fixed target coils inside the workspace. These fixed coils are used instead of the actual catheter prototype to mitigate the effect of other sources of error such as catheter modeling uncertainties.

The validation approach is different from the previously presented methods. In addition to same imaging plane orientation used during the calibration step, validation target coils are also imaged in other plane orientations to study the feasibility of the presented registration approach for multiplanar imaging capabilities of MRI. In this sense, [20] reports the closest validation method as in that study the imaging plane is adapted to automatically follow the motion of the fiducial frame in the scanner. In [20], only a single slice was used for registration, whereas this study utilizes multi-slice images to take full advantage of the 3D information in the registration.

III. MRI SCANNER TO CATHETER REGISTRATION

In this section, the employed approach to address the scanner to robot registration is presented. Fig. 2 and Table I define the coordinate systems used in the registration process.

In the proposed scheme, the registration will be performed with the help of a set of active artificial fiducials created in the MRI images. These active artificial fiducials will be in the form of localized MRI image artifacts created by passing electric currents through a set of electromagnetic coils, which will be referred to as "active fiducial coils." These coils act as "active" fiducial markers, rather than passive fiducial markers, because, it is possible to actively turn them on and off, allowing to control if and when these fiducial artifacts

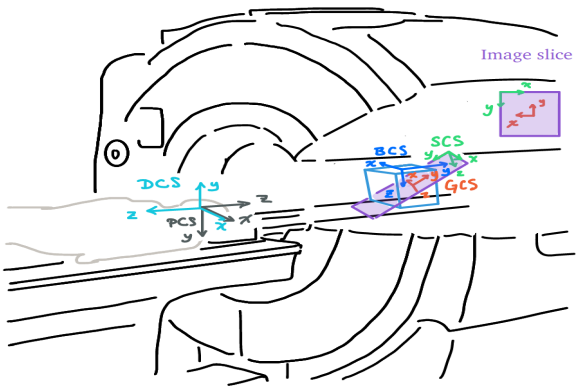


Fig. 2. Visualizes the coordinate systems defined for the registration process. DCS and PCS are drawn outside the bore for a cleaner visualization.

are created in the MRI images.

A. Problem Description

Suppose the ground truth locations of the fiducial coils in robot base coordinate system (BCS) are known from the CAD design file and represented as \bar{q}_B^j for $j \in \{1, \cdots, 8\}$. The same corresponding coils are detected in MRI scanner's device coordinate system (DCS) and are represented as \bar{q}_D^j for $j \in \{1, \cdots, 8\}$. The transformed the coil location from the device coordinate frame (DCS) to the base coordinate frame (BCS) are represented as:

$$\bar{q}_B^j = R_{BD}\bar{q}_D^j + t_{BD} \text{ with } j \in \{1, \dots, 8\},$$
 (1)

where R_{BD} represents the orientation of the DCS with respect to BCS and t_{BD} is the location of the origin of DCS with respect to BCS.

Then, the goal of the registration procedure is finding the optimum rigid transformation, which minimizes the distance between these two sets of corresponding points in the least-square sense.

$$\underset{[R_{BD}, t_{BD}]}{\operatorname{argmin}} \sum_{j=1}^{N} ||\bar{q}_{B}^{j} - \bar{g}_{BD}\bar{q}_{D}^{j}||^{2}, \tag{2}$$

where \bar{g}_{BD} is the homogeneous representation of $g_{BD} = (t_{BD}, R_{BD}) \in SE(3)^1$:

$$\bar{g}_{BD} = \begin{bmatrix} R_{BD} & t_{BD} \\ 0 & 1 \end{bmatrix}. \tag{3}$$

This homogeneous transformation matrix represents the mapping from scanner's device coordinate system to robotic catheter's base coordinate system. In (2), N is equal to the number of coils used. If all the fiducial coils are utilized, then N=8.

Thus, the first step of registering the MRI scanner to catheter base is detecting the fiducial coils in the scanner images. Flowchart of the registration procedure is given in Fig. 3.

B. Active Fiducial Coil Detection in MR Images

First, a multi-slice image is acquired when the coils are inactive. This image provides the background model. Then, the coils on top side of the pillars are activated by passing current through coils². Another multi-slice image is acquired using the same imaging sequence. This image provides the foreground model. As the only change in the scene is the activated coils, performing background subtraction gives an artifact, which corresponds to coil locations among the slices. This step is then repeated for the coils located at the bottom side of the pillars. The images for the background, foreground, and the result of background subtraction for the same slice is shown in Fig. 4.

For each coil, the size of the artifact is largest in the image slice that intersects the center of the coil, and the artifact size gradually decreases as the slices move away from center towards the edges of the coil. For each slice, the centroid and radius of the artifact are calculated by Hough Transform [35]. The fiducial artifacts for a set of multi-slice image are shown in Fig 5. With this information, area of the artifact in each slice is calculated and these areas are used to compute a weighted average of the centroids among slices to get the final detected coil location.

C. Mapping Detected Fiducial Coils to Scanner Device Coordinate System

The detected coil location from the weighted average computation is then mapped from slice coordinate system (SCS) to scanner's device coordinate system (DCS) by a sequence of homogeneous transformations given in (4):

$$\bar{q}_D = \bar{g}_{DP} \, \bar{g}_{PG} \, \bar{g}_{GS} \, \bar{q}_S \,. \tag{4}$$

In (4), \bar{q}_S is the detected coil in SCS in homogeneous coordinates and \bar{q}_D is the detected coil mapped to DCS. The descriptions of the coordinate systems corresponding to these

²Coil and applied current specifications are given in Section IV.

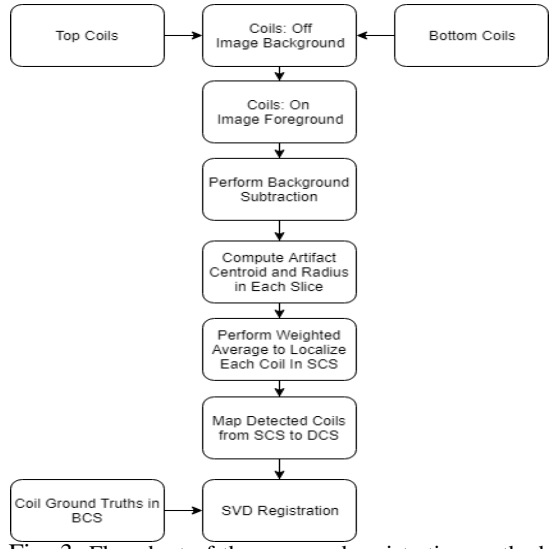


Fig. 3. Flowchart of the proposed registration method.

 $^{^{1}}SE(3)$ is the Special Euclidean group of \mathbb{R}^{3} [34].

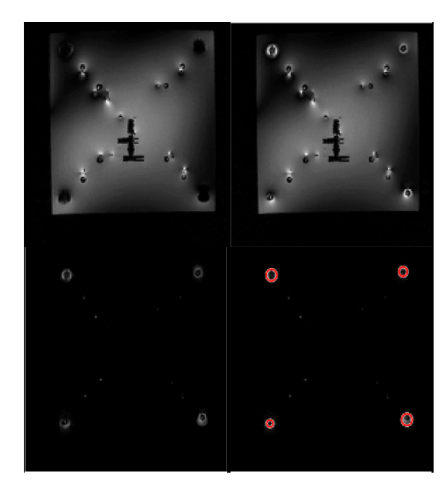


Fig. 4. Foreground (upper left), background (upper right), background subtracted (lower left), and coil detection (lower right) images (coronal orientation) for the same slice.

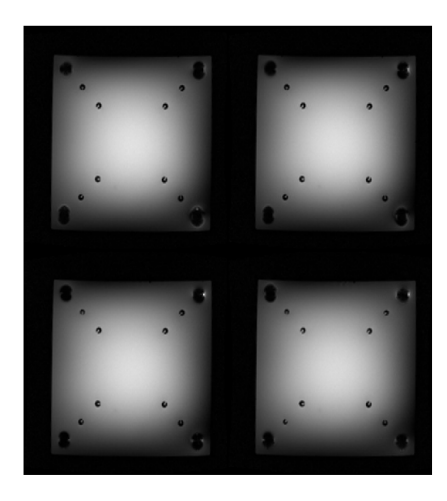


Fig. 5. Active fiducial coil artifacts in a multi-slice image (coronal orientation). Artifact size changes throughout the slices.

transformations are given in Table I. Plugging (4) in (2), \bar{g}_{BD} and thus mapping from DCS to BCS can be represented as:

$$\bar{q}_B = \bar{g}_{BS} \, \bar{g}_{SG} \, \bar{g}_{GP} \, \bar{g}_{PD} \bar{q}_D \,. \tag{5}$$

Applied magnetic field gradient coordinate system (GCS) is always at the center of the SCS and has a fixed orientation with respect to SCS. Thus, \bar{g}_{SG} is constant. Patient (sagittal, coronal, transverse) coordinate system (PCS) origin matches the origin of the DCS and has a fixed orientation with respect to DCS thus \bar{g}_{PD} is also constant. Only \bar{g}_{GP} changes with each slice in a multi-slice image in the direction of imaging plane with a magnitude of slice thickness. The transformations \bar{g}_{SG} , \bar{g}_{GP} , and \bar{g}_{PD} are known and provided by the scanner. Only unknown is \bar{g}_{BS} and is estimated by solving (2).

The detected coil location converted from pixel values to Cartesian coordinates based on the pixel resolution. As there are four fiducial coils located on the top pillars \bar{q}_D^j for $j \in \{1, \dots, 4\}$. Repeating the same procedure for the

TABLE I. Shows the notation for the coordinate systems, their corresponding acronyms and origins used in the document.

Frame Origin	Acronym	Coordinate System					
S	SCS	Slice Coordinate System					
G	GCS	Gradient Coordinate System					
D	DCS	Device Coordinate System					
P	PCS	Patient Coordinate System					
В	BCS	Base Coordinate System					

four bottom fiducial coils would give \bar{q}_D^j for $j \in \{5, \cdots, 8\}$. Thus, all the fiducial coils are mapped to DCS.

D. Least-Square Based Registration

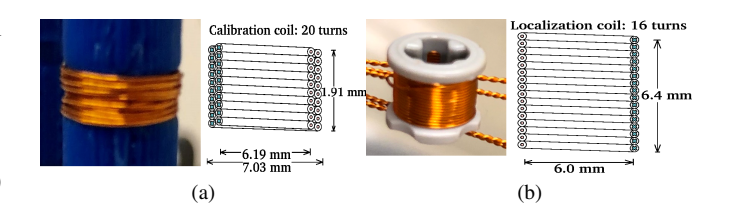
Once all the fiducial coils are mapped to DCS, the least-squares problem given in (2) can be solved. Registering two corresponding sets of three DOF data is a well-studied problem. In [36], Eggert discusses and compares previously introduced four algorithms [37]–[40] to solve this problem.

In this study, the singular value decomposition (SVD) based least-squares fitting algorithm proposed by Arun [39] is employed to find the optimum transformation. In short, first the centroids of both dataset are computed and then both datasets are centered around the origin. Optimal rotation R_{BD} in (3) is computed via applying SVD to the covariance matrix of the centered datasets. Plugging the optimal rotation and the centroids into the (1) gives the optimum translation t_{BD} . Sorkine [41] gives a concise summary of the algorithm.

IV. VALIDATION EXPERIMENTS

A. Experiment Setup

The calibration prototype (Fig. 6c) is embedded with 29 current-carrying coils (24 of them on pillars and 5 of them on tree structure), each of which is a 20-turn coil for pillars (Fig. 6a) and 16-turn coil (Fig. 6b) for tree structure. The coils are made of heavy insulated 30-gauge AWG magnet wires (Adapt Industries, LLC, Salisbury, MD, USA). The



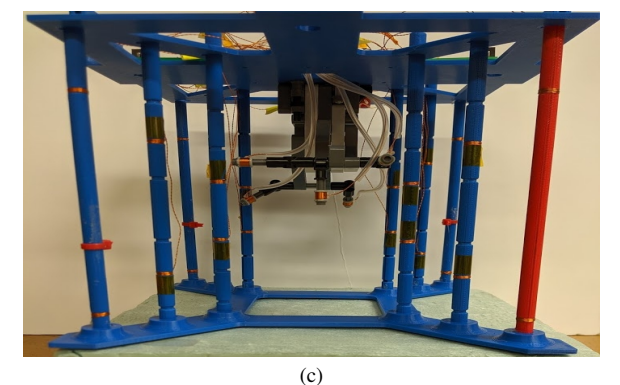


Fig. 6. (a) Registration coil. (b) Validation coil. (c) Registration frame prototype used in the experiments.



Fig. 7. Experiment setup inside a clinical MRI scanner. The Registration frame prototype is immersed in a phantom filled with distilled water doped with a gadolinium-based contrast agent. Phase array RF coils are placed on top of the prototype.

prototype itself is 3D printed with ABS-M30TM (Stratasys, Ltd, 7665 Prairie, MN, USA) material. The experiments are conducted in a 3T clinical scanner (Skyra, Siemens Medical Solutions, Erlangen, Germany), as shown in Fig. 7. The calibration prototype is mounted vertically inside an aquarium tank (25.4x25.4x26.7 cm³) and immersed in a phantom filled with distilled water doped with a gadolinium-based contrast agent. The aquarium tank is centered along the central axis of the MRI scanner and a phase array RF coil is placed on top of the prototype. The cables of the coils are connected to a transconductance amplifier controller which stays inside the MRI room outside the 5 Gauss line. The controller box sets the coil currents using a micro-controller which communicates with a PC located outside the MRI room through a USB serial link over fiber.

B. Experimental Methods

A differential multi-slice image registration algorithm is presented in Section III. The schematic in Fig. 1 visualizes the coils used in this study for both calibration and validation purposes. For this the following procedure was used.

- An initial scout image acquisition with a coarse resolution is performed to determine phantom location inside the bore.
- 2) The coils located on the top side of all the lattice pillars are scanned in coronal orientation. Outer pillar coils are used for calibration. Mid and inner pillar coils are reserved to use later for validation. A gradient echo acquisition with the following parameters is performed: Echo time (TE) = 4.62 ms, slice thickness = 1.5 mm; field of view = 300x300 mm; matrix size = 192x192; flip angle = 20 degrees; bandwidth = 260 Hz/pixel. This gives the background model explained in Section III. The acquisition is then repeated by activating the coils with a current of 75 mA.
- 3) Step 2 is repeated for the bottom coils.
- 4) The LEGO® made structure, located at the middle, embdes 5 coils, which are used for validation in addition to mid and inner pillar coils. This structure replaces the actual catheter prototype to minimize the effect of catheter model uncertainties in validation. In order to investigate how using different imaging plane orientations affect the accuracy of target localization,

TABLE II. Describes for each dataset the image plane orientations used in acquisition and the number of slices collected.

Experiment	Imaging Plane	Number of Slices					
Calibration Outer Pillar	Coronal	Top Coils: 60 Bottom Coils: 60					
Localization Mid Pillar	Coronal	Top Coils: 60 Bottom Coils: 60					
Localization Inner Pillar	Coronal	Top Coils: 60 Bottom Coils: 60					
Localization Tree	Coronal	60					
Localization Tree	Sagittal	100					
Localization Tree	Transverse	120					
Localization Tree	Double Oblique	120					

multiple datasets are collected with different image plane orientations. For each dataset, the number of slices and image plane orientations are given in Table II. For each set, acquision is performed with same background/foreground sequence in Steps 2-3.

5) Depending on the number of slices and slice orientation, 26-34 receiver coils were used and repetition time (TR) was 518, 863, or 1040 ms depending on the number of slices.

Three separate trials were conducted to collect three separate calibration and validation dataset to evaluate the repeatability of the proposed registration scheme. For the first trial, Siemens double oblique orientations correspond to T>S36.2>C-13.5, meaning transverse (T) tilted towards sagittal (S) by 36.2° then towards coronal (C) by -13.5°. For the second and third trials, double oblique orientations correspond to T>C38.3>S10.0. The fiducial coil registration algorithm is implemented in MATLAB® and the analysis is performed offline. The registration step takes approximately 1.75 seconds after the image acquisition step on an Intel® 3.40GHz quad-core CPU with 16GB RAM under Linux operating system.

C. Results

Fiducial registration error (FRE) and target registration error (TRE) described in [42], [43] are used to evaluate the system performance. FRE is the modified cost function of the optimization problem described in Eq. 2.

$$FRE = \sqrt{\frac{\sum_{j=1}^{N} ||\bar{q}_{B}^{j} - \hat{g}_{BD_{opt}}\bar{q}_{D}^{j}||^{2}}{N}},$$
 (6)

where $\hat{g}_{BD_{opt}}$ is the result of calibration step. TRE is used when a new set of target points $(\bar{p}_B^j, \bar{p}_D^j)$ for $j \in {1, \cdots, M}$ are used for validation.

$$TRE = \sqrt{\frac{\sum_{j=1}^{M} ||\bar{p}_{B}^{j} - \hat{g}_{BD_{opt}}\bar{p}_{D}^{j}||^{2}}{M}}.$$
 (7)

In Table III, for all three separate trials, FRE is given in row 1 calibration results and TRE is given in rows 2-7 for validation results. The average and maximum TRE values are calculated to be 2.49 mm and 2.89 mm, while, average and maximum FRE values are calculated to be 1.97 mm and 2.19 mm, respectively. For each step, imaging out-of-plane errors averaged over all coils for that step is also reported. Image out-of-plane axis corresponds to z-axis for the coronal,

TABLE III. For all three trials FRE of calibration step (Row 1) and TRE of validation step (Rows 2-7). Out-of-plane mean error across all coils for each step is also shown.

Experiment	Imaging Plane	Error [mm]			Out-of-Plane	
Experiment		Trial 1	Trial 2	Trial 3	Mean Error[mm]	
Calibration Outer Pillar	Coronal	1.807	1.911	2.192	1.2	
Localization Mid Pillar	Coronal	1.820	2.456	2.553	1.65	
Localization Inner Pillar	Coronal	1.847	2.168	2.229	1.5	
Localization Tree	Coronal	2.582	2.382	2.624	1.76	
Localization Tree	Sagittal	2.510	2.689	2.842	1.88	
Localization Tree	Transverse	2.704	2.595	2.898	1.91	
Localization Tree	Double Oblique	2.731	2.858	2.279	-	

x-axis for the sagittal, and y-axis in Cartesian coordinates for the transverse orientations. Out-of-plane errors are within 0.5 mm of the slice thickness (1.5 mm). The validation experiments performed with the same imaging plane orientation as in the calibration step (coronal), has higher accuracy. Though, the out-of-plane errors are comparable, coronal = 1.76 mm, sagittal = 1.88 mm, transverse = 1.91 mm.

Fig. 8 shows the error for each individual coil spatially as an error ellipsoid, where principle radii in x-y-z directions is proportional to component error magnitudes. Each radii is scaled by a factor of 4 for better visualization. The spatial accuracy plot shows the presented method is not particularly biased towards a direction within the experiment space.

This study utilizes multi-slice images to take full advantage of the 3D information in the registration. Multi-slice validation is compared to the single slice method to analyze effectiveness of this approach. For the single slice method, instead of performing a weighted average, the fiducial artifact with the largest area across the multi-slice image is selected for coil localization. Table IV shows the experiment results for single slice method.

The effects of using multi-slice approach were also tested for statistical significance by paired t-test. Multi-slice approach led to performance improvements in registration when compared to single slice method (p<0.0001).



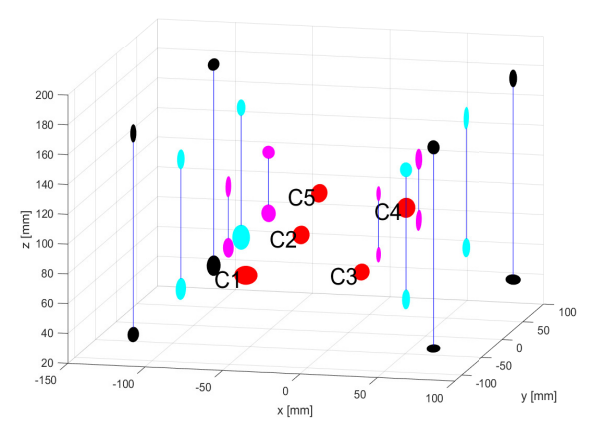


Fig. 8. Spatial visualization of coils and their error ellipsoids. Error ellipsoid principle radii in x-y-z directions is proportional to the component errors for each individual coil. Each radii is scaled by a factor of 4 for better visualization. Pillars of the structure also displayed in solid blue lines. C1:C5 labels the tree coils. Only the largest error among different imaging plane orientations are shown for tree coils.

TABLE IV. For all three trials FRE of calibration step (Row 1) and TRE of validation step (Rows 2-7).

· · · · · · · · · · · · ·								
Evnariment	Imaging Plane	Error [mm]						
Experiment	imaging i lane	Trial 1	Trial 2	Trial 3				
Calibration Outer Pillar	Coronal	2.311	2.356	2.592				
Localization Mid Pillar	Coronal	2.469	2.802	3.116				
Localization Inner Pillar	Coronal	2.344	2.949	3.020				
Localization Tree	Coronal	3.145	3.285	3.374				
	Sagittal	3.386	3.419	3.801				
	Transverse			3.712				
Localization Tree	Double Oblique	3.043	2.989	2.552				
	Localization Mid Pillar Localization Inner Pillar	Calibration Outer Pillar Coronal Localization Mid Pillar Coronal Localization Inner Pillar Coronal Localization Tree Coronal Localization Tree Sagittal Localization Tree Transverse	Experiment Imaging Plane Trial I Calibration Outer Pillar Coronal 2.311 Localization Mid Pillar Coronal 2.469 Localization Inner Pillar Coronal 2.344 Localization Tree Coronal 3.145 Localization Tree Sagittal 3.386 Localization Tree Transverse 3.612	Experiment Imaging Plane Trial 1 Trial 2 Calibration Outer Pillar Coronal 2.311 2.356 Localization Mid Pillar Coronal 2.469 2.802 Localization Inner Pillar Coronal 2.344 2.949 Localization Tree Coronal 3.145 3.285 Localization Tree Sagittal 3.386 3.419 Localization Tree Transverse 3.612 3.589				

V. DISCUSSION AND CONCLUSION

This study presents a differential multi-slice image based robot to MRI scanner calibration approach. Three separate trials were conducted to collect three separate calibration and validation datasets. The average registration and validation errors were respectively computed as 1.97 mm and 2.49 mm. Multi-slice images acquired in different orientations to investigate the effects of using different imaging plane orientations on the accuracy of target localization. The out-of-plane localizations were within 0.5 mm of the slice-thickness 1.5 mm. Multi-slice approach also compared to single-slice approach and is shown to have better registration performance (p<0.0001).

The number of separate trials for validation experiments could be increased to perform a more extensive repetability analysis. The registration performance analysis based on image acquisitions with different slice thickness would also be useful. It could be assumed the FRE and thus TRE would increase with increased slice thickness. Though, relative TRE performance with respect to FRE and slice thickness would be more informative. Thin slices needs a long duration to acquire to obtain a good signal to noise ratio. Therefore, it is desirable to get accurate registration also with thick slices [13]. This analysis remain as a future work. As the registration step would be performed once at the beginning of a clinical procedure. A thinner slice could be selected to achieve better performance, while accepting longer-acquisition times as a trade-off.

The future tests would include performing validation in the actual catheter prototype. This remains a future work as the framework for tracking the catheter prototype via MRI imaging is currently under development. Although the tree structure provides possible scenarios for actual catheter orientations, testing with the actual prototype would be more realistic for real-world clinical interventions. Finally, the impact of image quality on the accuracy of registration will be investigated in the future.

REFERENCES

- [1] What Is Catheter Ablation?, National Heart Lung and Blood Institute, http://www.nhlbi.nih.gov/health/health-topics/topics/ablation/.
- [2] J. Burgner-Kahrs, D. Rucker, and H. Choset, "Continuum robots for medical applications: A survey," IEEE Trans. Robot., vol. 31, no. 6, pp. 1261–1280, Dec 2015.
- K. Chinzei, N. Hata, F. A. Jolesz, and R. Kikinis, "Surgical assist robot for the active navigation in the intraoperative mri: hardware design issues," in *Proceedings. 2000 IEEE/RSJ International Conference on* Intelligent Robots and Systems, vol. 1, Oct 2000, pp. 727–732 vol.1.
- W. Kaiser, H. Fischer, J. Vagner, and M. Selig, Investigative Radiology.
- A. Krieger, G. Metzger, G. Fichtinger, E. Atalar, and L. L. Whitcomb, "A hybrid method for 6-dof tracking of mri-compatible robotic interventional devices," in Proceedings 2006 IEEE International Conference on Robotics and Automation, 2006. ICRA 2006., May 2006, pp. 3844-3849
- W. Shang and G. S. Fischer, "A high accuracy multi-image registration method for tracking mri-guided robots," vol. 8316, 2012. S. Lee, G. Fichtinger, and G. S. Chirikjian, "Numerical algorithms
- for spatial registration of line fiducials from cross-sectional images," Medical Physics, vol. 29, no. 8, pp. 1881-1891, 2002.
- R. C. Susil, J. H. Anderson, and R. H. Taylor, "A single image registration method for ct guided interventions," in Medical Image Computing and Computer-Assisted Intervention - MICCAI'99, C. Taylor and A. Colchester, Eds. Berlin, Heidelberg: Springer Berlin Heidelberg, 1999, pp. 798-808.
- S. P. DiMaio, S. Pieper, K. Chinzei, N. Hata, S. J. Haker, D. F. Kacher, G. Fichtinger, C. M. Tempany, and R. Kikinis, "Robot-assisted needle placement in open mri: System architecture, integration and
- validation," Computer Aided Surgery, vol. 12, no. 1, pp. 15–24, 2007.

 [10] S. Hushek, B. Fetics, and R. Moser, "Initial clinical experience with a passive electromagnetic 3d locator system," Interventional MRI Symposium, October 2004.
- A. Krieger, R. C. Susil, C. Menard, J. A. Coleman, G. Fichtinger, E. Atalar, and L. L. Whitcomb, "Design of a novel mri compatible manipulator for image guided prostate interventions," *IEEE Transac*tions on Biomedical Engineering, vol. 52, no. 2, pp. 306-313, Feb
- [12] J. A. Derbyshire, G. A. Wright, R. M. Henkelman, and R. S. Hinks, 'Dynamic scan-plane tracking using mr position monitoring,' of Magnetic Resonance Imaging, vol. 8, no. 4, pp. 924-932, 1998.
- A. Patriciu, D. Petrisor, M. Muntener, D. Mazilu, M. Schar, and D. Stoianovici, "Automatic brachytherapy seed placement under mri guidance," *IEEE Transactions on Biomedical Engineering*, vol. 54, no. 8, pp. 1499-1506, Aug 2007.
- [14] J. Tokuda, S.-E. Song, K. Tuncali, C. Tempany, and N. Hata, "Configurable automatic detection and registration of fiducial frames for device-to-image registration in mri-guided prostate interventions," Med Image Comput Comput Assist Interv, vol. 16, no. 3, p. 355–362, March
- [15] T. Liu, N. Lombard Poirot, T. Greigarn, and M. C. Cavuşoğlu, "Design of an mri-guided magnetically-actuated steerable catheter," ASME Journal of Medical Devices, Special Issue on Cardiovascular Device Development and Safety Assessment using Computational and/or Experimental Approaches, vol. 11, no. 2, p. 021004, 2017, cavusoglu:2015xg.
- [16] T. Liu and M. C. Cavusoglu, "Three dimensional modeling of an MRI actuated steerable catheter system," in *Proc. IEEE Int. Conf. Robot.* Autom., May 2014, pp. 4393-4398.
- [17] T. Liu, N. Lombard Poirot, D. Franson, N. Seiberlich, M. Griswold, and M. Cavusoglu, "Modeling and validation of the three dimensional deflection of an mri-compatible magnetically-actuated steerable catheter," IEEE Trans. Biomed. Eng., vol. PP, no. 99, pp. 1-1, 2016.
- [18] G. Li, H. Su, G. A. Cole, W. Shang, K. Harrington, A. Camilo, J. G. Pilitsis, and G. S. Fischer, "Robotic system for mri-guided stereotactic neurosurgery," *IEEE Transactions on Biomedical Engineering*, vol. 62, no. 4, pp. 1077-1088, April 2015.
- [19] R. Seifabadi, N. B. J. Cho, S.-E. Song, J. Tokuda, N. Hata, C. M. Tempany, G. Fichtinger, and I. Iordachita, "Accuracy study of a robotic system for mri-guided prostate needle placement," *The International* Journal of Medical Robotics and Computer Assisted Surgery, vol. 9, no. 3, pp. 305-316, 2013.
- S. P. DiMaio, E. Samset, G. Fischer, I. Iordachita, G. Fichtinger, F. Jolesz, and M. C. Tempany, "Dynamic mri scan plane control for passive tracking of instruments and devices," in Medical Image Computing and Computer-Assisted Intervention – MICCAI 2007.
- Berlin, Heidelberg: Springer Berlin Heidelberg. 2007, pp. 50–58.

 [21] C. J. Nycz, R. Gondokaryono, P. Carvalho, N. Patel, M. Wartenberg, J. G. Pilitsis, and G. S. Fischer, "Mechanical validation of an MRI compatible stereotactic neurosurgery robot in preparation for pre-clinical trials," in 2017 IEEE/RSJ International Conference on Intelligent Robots and Systems (IROS), 2017, pp. 1677–1684.

- [22] S. Song, N. B. Cho, G. Fischer, N. Hata, C. Tempany, G. Fichtinger, and I. Iordachita, "Development of a pneumatic robot for MRI-guided transperineal prostate biopsy and brachytherapy: New approaches," in 2010 IEEE International Conference on Robotics and Automation, may 2010, pp. 2580–2585. G. S. Fischer, I. Iordachita, C. Csoma, J. Tokuda, S. P. DiMaio, C. M.
- Tempany, N. Hata, and G. Fichtinger, "MRI-Compatible Pneumatic Robot for Transperineal Prostate Needle Placement," *IEEE/ASME* Transactions on Mechatronics, vol. 13, no. 3, pp. 295–305, jun 2008.
- A. de Oliveira, J. Rauschenberg, D. Beyersdorff, W. Semmler, and M. Bock, "Automatic passive tracking of an endorectal prostate biopsy device using phase-only cross-correlation," *Magnetic Resonance in Medicine*, vol. 59, no. 5, pp. 1043–1050, 2008.
- A. Krieger, I. I. Iordachita, P. Guion, A. K. Singh, A. Kaushal, Menard, P. A. Pinto, K. Camphausen, G. Fichtinger, and L. L. Whitcomb, "An mri-compatible robotic system with hybrid tracking for mri-guided prostate intervention," IEEE Transactions on Biomedical Engineering, vol. 58, no. 11, pp. 3049–3060, Nov 2011.
 [26] J. Tokuda, K. Tuncali, I. Iordachita, S.-E. Song, A. Fedorov, S. Oguro,
- A. Lasso, F. M. Fennessy, C. M. Tempany, and N. Hata, "In-bore setup and software for 3t MRI-guided transperineal prostate biopsy," *Physics*
- in Medicine and Biology, vol. 57, no. 18, pp. 5823–5840, sep 2012. A. Krieger, G. Metzger, G. Fichtinger, E. Atalar, and L. L. Whitcomb, "A hybrid method for 6-DOF tracking of MRI-compatible robotic interventional devices," in *Proceedings 2006 IEEE International Con*ference on Robotics and Automation, 2006. ICRA 2006., may 2006, p. 3844-3849.
- [28] D. Stoianovici, C. Jun, S. Lim, P. Li, D. Petrisor, S. Fricke, K. Sharma, and K. Cleary, "Multi-Imager Compatible, MR Safe, Remote Center of Motion Needle-Guide Robot," IEEE Transactions on Biomedical Engineering, vol. 65, no. 1, pp. 165-177, jan 2018.
- [29] D. Stoianovici, C. Kim, D. Petrisor, C. Jun, S. Lim, M. W. Ball, A. Ross, K. J. Macura, and M. E. Allaf, "MR Safe Robot, FDA Clearance, Safety and Feasibility of Prostate Biopsy Clinical Trial," IEEE/ASME Transactions on Mechatronics, vol. 22, no. 1, pp. 115-126, feb 2017.
- [30] J. Tokuda, L. Chauvin, B. Ninni, T. Kato, F. King, K. Tuncali, and N. Hata, "Motion Compensation for MRI-compatible Patient-mounted Needle Guide Device: Estimation of Targeting Accuracy in MRI-10 (2012). guided Kidney Cryoablations," Phys Med Biol, vol. 63, no. 8, p. 85010,
- [31] M. Li, A. Kapoory, D. Mazilu, B. Woody, and K. A. Horvath, "Cardiac interventions under MRI guidance using robotic assistance," in 2010 IEEE International Conference on Robotics and Automation, may 2010, pp. 2574-2579
- [32] C. L. Dumoulin, S. P. Souza, and R. D. Darrow, "Real-time position monitoring of invasive devices using magnetic resonance," Magnetic
- Resonance in Medicine, vol. 29, no. 3, pp. 411–415, 1993. R. C. Susil, K. Camphausen, P. Choyke, E. R. McVeigh, G. S. Gustafson, H. Ning, R. W. Miller, E. Atalar, C. N. Coleman, and C. Ménard, "System for prostate brachytherapy and biopsy in a standard 1.5 t mri scanner," Magnetic Resonance in Medicine, vol. 52, no. 3, pp. 683-687, 2004.
- [34] R. M. Murray, Z. Li, and S. S. Sastry, A Mathematical Introduction to Robotic Manipulation, 1st ed. Boca Raton, FL: CRC Press, 1994.
- [35] D. Ballard, "Generalizing the hough transform to detect arbitrary shapes," *Pattern Recognition*, vol. 13, no. 2, pp. 111 – 122, 1981. [36] D. Eggert, A. Lorusso, and R. Fisher, "Estimating 3-d rigid body
- transformations: a comparison of four major algorithms," Machine Vision and Applications, vol. 9, no. 5, pp. 272–290, Mar 1997.
 [37] B. K. P. Horn, "Closed-form solution of absolute orientation using
- unit quaternions," J. Opt. Soc. Am. A, vol. 4, no. 4, pp. 629–642, Apr
- [38] B. K. P. Horn, H. M. Hilden, and S. Negahdaripour, "Closed-form solution of absolute orientation using orthonormal matrices," J. Opt. Soc. Am. A, vol. 5, no. 7, pp. 1127–1135, Jul 1988.
- [39] K. S. Arun, T. S. Huang, and S. D. Blostein, "Least-squares fitting of two 3-d point sets," *IEEE Transactions on Pattern Analysis and* Machine Intelligence, vol. PAMI-9, no. 5, pp. 698-700, Sep. 1987.
- [40] M. W. Walker, L. Shao, and R. A. Volz, "Estimating 3-d location parameters using dual number quaternions," CVGIP: Image Understanding, vol. 54, no. 3, pp. 358 – 367, 1991.
- standarg, Vol. 54, no. 5, pp. 538 361, 1991.
 [41] O. Sorkine, "Least-squares rigid motion using svd," Technical Notes, vol. 120, pp. 1–5, 2009. [Online]. Available: https://igl.ethz.ch/projects/ARAP/svd_rot.pdf
 [42] J. M. Fitzpatrick, J. B. West, and C. R. Maurer, "Predicting error in rigid-body point-based registration," IEEE Transactions on Medical Imaging, vol. 17, no. 5, pp. 694–702, Oct 1998.
 [43] P. B. Shopir, L. Joskowicz, and V. Shocken, "Fiducial optimization
- [43] R. R. Shamir, L. Joskowicz, and Y. Shoshan, "Fiducial optimization for minimal target registration error in image-guided neurosurgery," *IEEE Transactions on Medical Imaging*, vol. 31, no. 3, pp. 725–737, March 2012.